Simulation of First-Charge Oxygen-Dimerization and Mn-Migration in Li-rich Layered Oxides $x\mathrm{Li_2MnO_3}\bullet(1\text{-}x)\mathrm{Li}M\mathrm{O_2}$ and implications for Voltage Fade

Roy Benedek* and Hakim Iddir

Argonne National Laboratory, Argonne, IL 60439

Abstract

The instabilities of Li-rich layered oxide $x\mathrm{Li_2MnO_3}\bullet(1\text{-}x)\mathrm{Li}M\mathrm{O_2}$ (lithium-ion-battery cathode materials) during the first charge are investigated using first-principles dynamical simulation. To complement our earlier simulations for (x = 0.4, M = $\mathrm{Ni_{0.5}Mn_{0.5}}$), we address here: pure $\mathrm{Li_2MnO_3}$; small x; M compositions that include Co; a composite with Co spinel: $\mathrm{Li_2MnO_3}\bullet\mathrm{Li_2}M_2\mathrm{O_4}$; a $\mathrm{Li_2MnO_3}$ slab. We discuss how the threshold fraction f of $\mathrm{Li_{2(1\text{-}f)}MnO_3}$ delithiation at which instabilities occur at the surface, f_{th}(surface), differs from that in the bulk, f_{th}(bulk). Approaches to inhibit voltage fade are discussed.

I. Introduction

Li-rich layered oxides[1-3] $x\mathrm{Li_2MnO_3}\bullet(1\text{-}x)\mathrm{Li}M\mathrm{O_2}$, where M = Ni, Co, Mn, …, yield extraordinarily high capacities as cathode materials in Li-ion batteries (as high as 300 mAh/g [4]), but suffer from structural instabilities that lead to voltage fade upon cycling[3, 5]. The high capacities, well in excess of those available in $\mathrm{Li}M\mathrm{O_2}$, are attributed largely to (i) the high Li density in the $\mathrm{Li_2MnO_3}$ component, which becomes electrochemically active at voltages above $V_a \approx 4.45$, and (ii) the stabilizing effect of the $x\mathrm{Li_2MnO_3}\bullet(1\text{-}x)\mathrm{Li}M\mathrm{O_2}$ mixture against phase transitions that occur during charging of the end members (x=0 or x=1). Nevertheless, unless the voltage fade (*VF*) can be substantially lowered (perhaps to the order of 0.1 mV/cycle, much lower than has been achieved to date [3][3]), it is doubtful that the Li-rich layered oxides will be employed in transportation applications[6], despite their high capacities. Improved understanding and characterization of the mechanisms responsible for voltage fade, however, may suggest strategies to make the Li-rich materials viable. On the basis of previous simulations[7-8], complemented by those presented here, we argue that stabilization of the surface against structural instabilities that result in transformations to lower-energy-density materials, if possible, combined with restricted upper cutoff voltages ($V_c < \approx 4.6$), may be the only way to achieve this objective. Thus, the structural damage (high oxygen-dimer and migrated-Mn densities) introduced into the bulk, as well as at the surface, of the Li-excess materials after full first-cycle activation ($V_c \approx 4.8$), is likely so profound that no tuning of the composition, synthesis procedures, etc., would yield satisfactory cycling performance.

A general understanding is emerging of the structural instabilities induced by delithiation during the first charge and the resultant transformations of the material, which are intimately tied to the charge compensation process during delithiation. In the early part of the first charge, Li is extracted primarily from the $\mathrm{Li}M\mathrm{O_2}$ component of the system, and charge compensation occurs by oxidation of M ions (in the vicinity of the extracted Li), albeit with some participation of oxygen, particularly in the case of Co[9-11]. (Simulation[12] suggests that the very first delithiation events upon charge occur at the $\mathrm{Li_2MnO_3}$-$\mathrm{Li}M\mathrm{O_2}$ interfaces, however, the contribution of such events to the capacity may be small, and have not been identified in experiment.) The fraction of Li extracted from the $\mathrm{Li}M\mathrm{O_2}$ component in this step is thought to be of order 0.6 - 0.8, based on the location of the point of inflection near V_a in the first charge voltage vs. capacity curve. This portion of the first charge, although somewhat destabilizing, still leaves the bulk framework structure, including the M sublattice, substantially intact.

Further delithiation, at voltages higher than V_a, results in charge compensation by anion oxidation on the $\mathrm{Li_2MnO_3}$ component, in which oxygen in the 1– oxidation state is created. A considerable effort has been made to characterize the anion redox process. Theory[13-15] indicates that octahedral oxygen is vulnerable to oxidation when it possesses non-bonding O2*p* lone-pair orbitals. In the pristine material, non-bonding ($2p_x$, $2p_y$, or $2p_z$) axes coincide with linear Li-O-Li trimer axes. Such trimers occur in bulk $\mathrm{Li_2MnO_3}$, but not $\mathrm{Li}M\mathrm{O_2}$ (in the absence of Li-M exchange). In pristine $\mathrm{Li_2MnO_3}$, oxygen is stabilized in the 2- oxidation state partly by chemical bonding, and partly by the crystal field. The non-bonding axes, however, are responsible for high-lying O2*p* spectral features[13-15]. Oxidation of the oxygen ion at the center of the trimer occurs upon removal of a non-bonding-axis Li. Thus, charging $x\mathrm{Li_2MnO_3}\bullet(1\text{-}x)\mathrm{Li}M\mathrm{O_2}$ to voltages above V_a results in the creation of $\mathrm{O^{1-}}$, i.e., holes on oxygen ions.

With a Li ion removed from an Li-O-Li trimer, crystal-field stabilization of the oxygen sublattice is weakened, and bonding of an oxidized $\mathrm{O^{1-}}$ ion to its original lattice site is degraded. When the density of $\mathrm{O^{1-}}$ reaches a threshold, the energy can be lowered by oxygen-ion displacement to form peroxide, superoxide, or molecular O-O dimers. The rearrangement of the oxygen sublattice results in lowering the barriers to Mn migration, and therefore leads to further structural transformations[7]. Although oxygen dimerization is expected primarily in the $\mathrm{Li_2MnO_3}$ component, destabilization of the $\mathrm{Li}M\mathrm{O_2}$ component owing to oxygen oxidation at high states of charge may lead to some oxygen rearrangement in that component as well [16].

Despite the weakened bonding of O^{1-} ions to the lattice, barriers exist to dimerization, and when the charge voltage is restricted to be only moderately above V_a, and the resultant density of O^{1-} ions is not too high, the oxygen sublattice remains intact. The behavior at Li_2MnO_3 surfaces differs from that in the bulk: barriers to dimerization, sublimation, and/or Mn migration, either vanish or are much smaller in the vicinity of a surface (cf. section III.D). The surface transformations lead, upon cycling, to spinel formation[17]. Despite the observation of spinel at the surface[17], details of the spinel nucleation and growth process, either at the surface or in the bulk[18], remain unknown. The relative contribution of surface transformations and bulk transformations to the nucleation of low-energy-density phases (and *VF*) is therefore poorly understood. For example, even if the surface transformations could be suppressed, the bulk transformations following full activation would destroy the atomic ordering in Li_2MnO_3 domains, and consequently degrade the energy density, although the presence of oxygen dimers in the bulk may hinder spinel nucleation.

The picture we have summarized of how disorder is introduced with the creation of oxygen dimers and migrated Mn during the first charge appears to be widely accepted, but does not in itself have predictive capability, either of the density of defects or of the creation of new lower energy-density phases. The presence of a spectrum of energy barriers to atomic rearrangement motivates the application of dynamical simulation methods.

In our previous work[7-8], dynamical simulations were performed for the first charge of a Li-rich system with $M = Ni_{0.5}Mn_{0.5}$. An atomic arrangement[12] of the pristine material with alternating stripes of Li_2MnO_3 and $LiMO_2$ was assumed. The simulated results for x-ray spectroscopies (EXAFS analysis of *M* coordination, XRD (003) line intensity, and Rietveld refinement analyses of oxygen vacancies) reproduced the general features of the experimental measurements[7-8].

In the present work, the simulations of $xLi_2MnO_3\bullet(1-x)LiMO_2$ were extended to different choices of *M*, and *x*, as well as different atomic arrangements, to explore the effect of these parameters on the first-charge instabilities of the lithium-rich materials**.** Furthermore, we also perform simulations for a Li_2MnO_3 slab to investigate the influence of a free surface on the first-charge instability.

Based on the simulations, we discuss prospects for achieving low *VF*.

II. Model Description and Simulation Method

A. Atomic Arrangement

Except for *x* close to 0 or 1, it is assumed that pristine material decomposes into domains with Li_2MnO_3 and $LiMO_2$ atomic ordering during synthesis. As mentioned earlier, our previous simulations[7-8] considered parallel stripe domains a few atomic rows thick. Opinion remains divided, however, as to whether the pristine material should be regarded as a solid solution[19] or a composite [12]. In our opinion, a thermodynamic solid solution cannot exist in the presence of bonding energy scales as disparate as those for Li_2MnO_3 and $LiMO_2$[12]. It seems possible, however, that the decomposition (domain coarsening) that would ordinarily be expected in a two-phase material is defeated by sluggish kinetics, and that only local equilibrium with short range Li-Mn ordering is established, with Li ions in the metal layers surrounded predominantly by six Mn ions. Domain coarsening beyond the nano-scale appears not to occur on a laboratory time scale[20]. We suggest that most *M*-layer atomic arrangements of $xLi_2MnO_3\bullet(1-x)LiMO_2$ that incorporates Li-Mn short-range order may be reasonable approximations to the structure of these materials. For convenience, we have employed the parallel-stripe model used in earlier work in most of the calculations described here.

B. Transition metal composition *M* and Li_2MnO_3 fraction *x*

A great deal of work has been devoted to compositions $M = Ni_{(1-z)/2}Mn_{(1-z)/2}Co_z$, which exploit the stability of divalent, tetravalent and trivalent oxidation states of the respective constituents[21]. Here, we consider *M*=Co, $Co_{1/3}Ni_{1/3}Mn_{1/3}$, and $Co_{1/2}Ni_{1/4}Mn_{1/4}$ to complement earlier calculations on $M = Ni_{0.5}Mn_{0.5}$. In the simulations[7-8] for $M = Ni_{0.5}Mn_{0.5}$ we considered x=0.4, and Li_2MnO_3 and $LiMO_2$ stripes 4 atomic rows wide; we have adopted analogous structures in most of the simulations presented here.

The assumed pristine structures of $0.4Li_2MnO_3\bullet0.6LiCoO_2$ and $0.4Li_{2(1-f)}MnO_3\bullet0.3Li_2Co_2O_4$ are illustrated in Figs. 1 and 2.

To gain insight into the effect of smaller Li_2MnO_3 fractions, we considered the composition with x=0.1. In this case, we treated a structure with isolated linear Mn-Li-Mn trimers embedded in a Co background to form $0.1Li_2MnO_3\bullet0.9LiCoO_2$.

C. Non-bonding O2*p* Li-O-Li orbital axes

As mentioned above, non-bonding O2*p* orbitals along Li-O-Li axes have relatively high energy[13-15], and are therefore available to participate in charge compensation during the first charge at voltages above V_a. In our model structure, with domains that consist of parallel stripes of Li_2MnO_3 and $LiMO_2$, with x=0.4, half of the oxygen ions, those within the $LiMO_2$ domains, have no non-bonding Li-O-Li axes, whereas the oxygen ions within the Li_2MnO_3 domains each have one non-bonding oxygen axis. Non-bonding Li-O-Li axes require Li ions in the *M* layer, each of which is associated with 6 Li-O-Li axes. Therefore, in effect, each *M*-layer Li destabilizes six O ions, which are susceptible to migration or displacement if barriers to such motion are surmounted. A more complicated arrangement is obtained by considering, in place of the $R\bar{3}m$ structure of $LiMO_2$, the lithiated spinel[22] $Li_2M_2O_4$, which contains *M*

ions in the Li layer and vice versa, in the LiMO$_2$ component. One may view the atomic arrangement of the lithiated spinel as derived from the $R\bar{3}m$ structure by mixing the M and L layers: the M layer →Li$_{1/4}M_{3/4}$ and the Li layer →Li$_{3/4}M_{1/4}$. In bulk Li$_2M_2$O$_4$, as in bulk LiMO$_2$, no non-bonding Li-O-Li axes are present. For the Li$_2$MnO$_3$•Li$_2M_2$O$_4$ composite, however, owing to the Li ions in the Li$_{1/4}M_{3/4}$ layers of Li$_2M_2$O$_4$, some of the oxygen ions at the interface between LiMO$_2$ and Li$_2M_2$O$_4$ domains have two non-bonding Li-O-Li axes; in the Li$_2$MnO$_3$•LiMO$_2$ system, no oxygen ion had more than one Li-O-Li axis. This suggests that Li$_2$MnO$_3$•Li$_2M_2$O$_4$ may be more susceptible to oxygen dimerization than Li$_2$MnO$_3$•LiMO$_2$, during the first charge, and this is borne out by the simulations presented below.

D. Slab Geometry

The greater stability of the oxygen sublattice of xLi$_2$MnO$_3$•(1-x)LiMO$_2$ in the bulk than at a surface or interface may be attributed in part to the higher density of nonbonding O 2p axes at the surface, which leaves oxygen ions vulnerable to displacement, dimerization, sublimation and rebonding. To simulate this effect, we have considered a slab of Li$_2$MnO$_3$ with slab normal oriented perpendicular to the crystal layers. For simplicity, the slab is constructed with $R\bar{3}m$ (rather than monoclinic) symmetry. Slab terminations on a LiMn layer are considered for illustration. The coordination deficit of Mn ions in the termination layers enables them to rearrange spontaneously, along with oxygen, to form tetrahedral complexes.

E. Computational Model

The periodic unit cell employed in the bulk simulations includes 384 (=8x6x8) lattice sites, with 8 layers (2 Li, 2 M and 4 O layers) each of dimension 6x8 (6 atomic sites along close packed rows, with 8 such close-packed rows). Note however that Figs. 2-4, which include periodic replicas, show than 6 sites along the x axis.

Dynamical and static calculations were performed with the PAW implementation of the VASP code[23-24] at the GGA+U level, with the PBE correlation functional[25]. We selected $U_{\rm eff}$ = 4, 5, 5.9, 1 eV for Mn, Co, Ni, and Ru, respectively[7-8]. Higher-level treatments, e.g., with HSE hybrid density functionals[26], are available, however, the large cell sizes employed in this work would make such treatments prohibitive. A single k-point is employed in all calculations presented[7-8].

As in our previous work[7-8], the present dynamical simulations were performed at T=1000 K, to accelerate the dynamics, compared to that at ambient temperatures. The VASP code employs a Verlet algorithm to update atomic coordinates at each time-step. The selected MD time-step was 1 fs. The simulations for each composition were continued until an asymptotic value of the number of oxygen dimers was reached, and the system appeared close to a steady state. In some cases, only a few ps was sufficient to approach approximately steady state conditions, whereas for M=Ni$_{0.5}$Mn$_{0.5}$, the simulations were continued for more than 30 ps.

The activation barrier $E_{\rm a}$ for oxygen dimerization in Li$_{2(1-f)}$MnO$_3$ obtained from our dynamical simulation (cf. section IIIA), agrees closely with that derived from static calculations along hypothetical reaction paths[15]. This agreement provides some corroboration for our treatment.

F. Dimerization Threshold f_{th}

The composition at a given state of delithiation during the first charge is represented as

$$x\text{Li}_{2(1-f)}\text{MnO}_3\bullet(1-x)\text{Li}_y M\text{O}_2, \qquad (1)$$

where f and 1-y represent the delithiation fractions of the Li$_2$MnO$_3$ and LiMO$_2$ components, respectively. As mentioned in the introduction, it appears that, prior to activation, the LiMO$_2$ component delithiates to approximately $y(V_a)$ = 0.2-0.4. In simulations, we assume for convenience that y = 0 at the onset of activation; if this overestimates the delithiation of LiMO$_2$, the system can equilibrate by migration of Li from the Li$_2$MnO$_3$ region to the LiMO$_2$ region, which does occur to a small extent.

Oxygen dimerization during the first charge depends sensitively on f. At low values of f, no driving force exists for dimerization, and only above a threshold value, f_{th}(bulk), does dimerization become appreciable. In our previous simulations[7-8] for M = Ni$_{0.5}$Mn$_{0.5}$, we found f_{th}(bulk) ≈ 3/8.

Because $y(V_a) > 0$, simultaneous delithiation of Li$_y M$O$_2$ and Li$_{2(1-f)}$MnO$_3$ may occur for $V > V_a$, which may affect f_{th}. We do not address this complication in the present work.

Since electrode surface (or interface) ions are under-coordinated, we expect greater instability at the surface, and therefore f_{th}(surface) < f_{th}(bulk). The less constrained environment at a surface, relative to the bulk, enables transformations other than oxygen dimerization when f > f_{th}(surface), as discussed in section II.E, in which slab calculations are presented.

As in our previous simulations, we have adopted the value f = ¾ in most of the present bulk calculations, which corresponds to removal of an amount of Li equal to the Li content of the Li layers. This choice corresponds to a state of charge close to the end of the voltage plateau.

III. Results

A. x=1: pure Li$_{2(1-f)}$MnO$_3$

First principles dynamical (MD) simulations were performed pure Li$_{2(1-f)}$MnO$_3$, at temperature T = 1000 K to obtain the dimerization fraction $n_{\rm dim} = n(\text{O}_2)/n_{213}(\text{O})$ as a function of simulation time, t, where $n(\text{O}_2)$ is the number of oxygen dimers (which we define here as the number of oxygen pairs with bond length less than 1.7 Å) and n_{213}(O) is the number of oxygen ions in the Li$_2$MnO$_3$ component;

$n_{213}(O)/n(O) = 3x/(x+2)$, where $n(O)$ is the total number of oxygen ions. $n_{213}(O)/n(O)=1$, for pure Li_2MnO_3.

To estimate the expected range of n_{dim}, consider the case in which all dimers are peroxo species, so that dimers are created in oxidation state 2-. If the holes from $2f$ electrons per $Li_{2(1-f)}MnO_3$ formula unit removed by delithiation are distributed among f peroxo dimers (O_2^{2-}), a density (per oxygen atom in the $Li_{2(1-f)}MnO_3$ component of the material) $n_{dim}= f/3$ would be formed. Distribution of the holes entirely on neutral O_2 dimers would give $n_{dim}= f/6$. We consider $f=3/4$ to represent, essentially, the end of the first charge plateau, and thus the maximum expected density of dimers (in the $Li_{2(1-f)}MnO_3$ component of the material) is $n_{dim}(max)= ¼$, at least in the case of pure $Li_{2(1-f)}MnO_3$. $n_{dim}(max)$ should not be viewed as an absolute upper bound in $xLi_{2(1-f)}MnO_3\bullet(1-x)Li_yMO_2$, however, because of possible instability in the Li_yMO_2 component. In order to make comparisons between simulation results and this value, we normalize n_{dim} to the density of oxygen in the $Li_{2(1-f)}MnO_3$ component, $n_{213}(O)$, rather than $n(O)$, throughout.

Results for $n_{dim}(t)$ are plotted in Fig. 3. The time dependence of $n_{dim}(t)$ can be represented approximately by the exponential

$$n_{dim}(t) = n_{dim}\,[1 - \exp(-t/t_o)], \qquad (2)$$

where n_{dim} and t_o are constants. The asymptote $n_{dim} = n_{dim}(t=\infty)$ may be viewed as the equilibrium concentration of dimers. If the kinetics at $t=0$ were governed by a single activated process with activation barrier E_a, then

$$dn_{dim}(t)/dt\,|_{t=0} = n_{dim} / t_o \approx 3\,\nu\,\exp(-E_a/k_bT), \qquad (3)$$

where ν is an effective vibrational frequency, and the factor of 3 accounts for the number of spatial dimensions. A fit of the data in Fig. 3 to Eq.(3), with $\nu = 10^{13}$ sec^{-1}, yields $E_a = 0.61$ eV. This effective energy barrier is almost identical to that obtained by static simulations of the reaction path for the dimerization of oxygen ions in adjacent layers[15].

The actual physics of the first charge instabilities is undoubtedly more complicated than Eqs. (2) and (3) would suggest, however these relations enable us to filter out much of the noise in the dynamical simulations, so that fitted values of n_{dim}, t_o, and E_a for the different systems can be compared with each other. We note, however, that accurate determination of n_{dim} by fits to Eq.(2), require extension of the simulation well into the asymptotic regime (a few times t_0, say), which is costly; otherwise a more accurate estimate of n_{dim} can be made by inspection of the $n_{dim}(t)$ curve.

The density of dimers $n(O_2)$ includes peroxide, superoxide and molecules. These dimer types may be distinguished from each other by whether both, one, or neither member of the oxygen dimer remains bonded to at least one metal ion. For molecules, dimer bond lengths in the range of 1.2 Å are found, whereas for peroxide, values as high as about 1.7 Å are found. This is illustrated in Fig. 4, which shows a distribution of dimer bond lengths (relative probability that a given dimer resides in a bond length interval of 0.01 Å) for $xLi_{2(1-f)}MnO_3\bullet(1-x)Li_yMO_2$, in the case of $M=Ni_{0.5}Mn_{0.5}$, for $x=0.4$, $f=3/4$, $y=0$. The plotted points were obtained by superposition of results for several hundred time-steps, late in the MD simulations for $M=Ni_{0.5}Mn_{0.5}$ ($t \sim 30$ ps), after the system had achieved near steady-state conditions. The smallest dimers ($r_{dim} \sim 1.2$ Å) have bond lengths in the range expected for neutral O_2, whereas the largest ones are slightly larger than would be expected for isolated peroxide molecules. Similar spectra for $n(r_{dim})$, with r_{dim} lying primarily in the range between 1.2 and 1.7 Å. are found for choices of M other than $Ni_{0.5}Mn_{0.5}$. In the case of small x (cf. section C), a different atomic arrangement of Li and Mn in the M layer is assumed; in that case, peaks in the $n(r_{dim})$ spectrum, centered at a few discrete values of r_{dim} in the range between 1.2 and 1.7 Å occur.

B. x=0.4: parallel stripes of Li_2MnO_3 and $LiMO_2$

Dynamical simulations were performed for systems that contain Co, e.g., M=Co and $M=Co_{1/3}Ni_{1/3}Mn_{1/3}$, to investigate the effect of Co on dimerization. Analysis of the simulation results using Eqs. (2) and (3) showed smaller t_o, E_a, and n_{dim} than those for $z=0$ ($M=Ni_{0.5}Mn_{0.5}$). Thus, the presence of Co^{4+}, created by the delithiation of the Li_yMO_2 component ($y=0$), appears to lower energy barriers for oxygen dimer formation in the $Li_{2(1-f)}MnO_3$ domains, but also lowers the equilibrium density of dimers created. Thus. $E_a = 0.66$ (0.53) and $n_{dim}= 0.23$ (0.16) for $M=Ni_{0.5}Mn_{0.5}$ (Co). The Li layers of the pristine materials are assumed pure in these simulations, with no Li-M exchange[27]. These values of n_{dim} are lower than the estimated upper bound $n_{dim}(max)= ¼$, as expected; see, however, section C, for further discussion.

One may wonder whether the present results suggest that the inclusion of some Co in M is beneficial. It is difficult to draw a conclusion from the simulation alone, because we are unable to continue the simulation beyond the first charge. As is discussed below, however, we believe that low VF-operation, if feasible, is likely only possible for $f < f_{th}$(bulk), so that dimerization in the bulk is suppressed; cf. section IV.

The Co-bearing system $LiCoO_2$ is known to exhibit a low temperature polymorph with the structure of lithiated spinel ($Li_2Co_2O_4$). As mentioned above, this structure differs from *R-3m* in that ¼ of the Li in the Li layer are exchanged with Co in the M layer. This system has received attention in the context of layered-layered-spinel (LLS) composites[28]. We have performed simulations for the layered-spinel system $xLi_{2(1-f)}MnO_3\bullet(1-x)0.5Li_2Co_2O_4$. Whereas $n_{dim}\sim 0.15$ for $xLi_{2(1-f)}MnO_3\bullet(1-x)LiCoO_2$, $n_{dim}\sim 0.35$ for $xLi_{2(1-f)}MnO_3\bullet(1-x)0.5Li_2Co_2O_4$. Thus, n_{dim}

exceeds the estimated upper bound $n_{dim}(max)$= ¼ for pure $Li_{2(1-f)}MnO_3$. The Co ions in the Li layer of the spinel component $Li_2Co_2O_4$, thus tend to stabilize oxygen dimers during first-charge activation.

Figure 2 presents a snapshot from the dynamical simulation for $xLi_{2(1-f)}MnO_3$•$(1-x)Li_yCoO_2$ (x=0.4, f = ¾, y=0) after t = 5 ps, when the number of oxygen dimers has essentially reached a steady state. The $LiCoO_2$ component (with Co ions blue) is at the left-hand side of the figure (small y), and the $Li_{2(1-f)}MnO_3$ component is at the right-hand side. The periodic unit cell contains 8 atomic layers (2 Li, 2 LiM and 4 O layers), with 384 lattice sites, but some atoms at the edges are duplicated in the figure. The remaining Li ions (green) are primarily in the Li layers of the $Li_{2(1-f)}MnO_3$ regions, as are the majority of the oxygen dimers (bond length < 1.7 Å). Comparing Fig. 5 with Fig. 0a, we observe that delithiation in the first charge has resulted in the creation of dimers that occupy both the $Li_{2(1-f)}MnO_3$ and the $LiCoO_2$ regions. Further, we see warping of the atomic rows of O and Mn, as well as disordered Li that occupies primarily the $Li_{2(1-f)}MnO_3$ region.

Fig. 6 shows a snapshot of $xLi_{2(1-f)}MnO_3$•$(1-x)0.5Li_2Co_2O_4$ (x=0.4, f = ¾, y=0), when that system had essentially reached steady state. In contrast to Fig. 5, Li ions, as well as oxygen dimers, reside on the $Li_2Co_2O_4$ side (small y) of the system. The presence of Co ions in the Li layer of $Li_2Co_2O_4$, which is essentially the only difference between $LiCoO_2$ and $0.5Li_2Co_2O_4$ (cf. Figs. 1 and 2), thus appears to attract oxygen dimers. This phenomenon will tend to promote activation during the first charge of LLS integrated materials[22].

C. Small *x*: behavior for *x*=0.1

In the limit of small x, Li_2MnO_3 domains are expected to be small. To simulate the small x limit, we consider isolated linear Mn-Li-Mn trimers embedded in the M layers of xLi_2MnO_3•$(1-x)LiMO_2$, with x=0.1. Such an atomic arrangement would be consistent with the solid solution picture. For M=Co, our dynamical simulations indicate that dimers form relatively easily upon activation (all Li removed from Li layers). Analysis of the simulations yields a small effective barrier E_a = 0.35 eV, and a high equilibrium concentration of dimers, n_{dim} = 0.45. A snapshot of this system after t = 3 ps is shown in Fig. 7. Most of the oxygen dimers are located close to Mn ions (purple).

The results of this simulation, particularly the small effective barrier E_a, suggest that the limit of small x, with atomic structure that mimics a solid solution, confers less structural stability during first charge than higher values of x. This instability is also reflected in the high dimer density, which exceeds our estimated upper bound $n_{dim}(max)$= ¼.

D. Mn migration

As mentioned in the introduction, oxygen dimerization lowers the barrier for Mn migration. Only after a threshold concentration of oxygen dimers is reached does Mn migration become appreciable[7]. In the spirit of Eq. (1), we consider an idealized exponential form, but with a time delay t_d:

$$n_{Mmig}(t) = H(t-t_d)\, n_{Mmig}\, [1 - \exp(-[t-t_d]/t_M)], \qquad (4)$$

where $H(t)$ is the Heaviside step function. Eq.(4) reduces to the same form as Eq.(1) if t_d =0. Our numerical results indicate that $t_d \approx t_o/2$, $n_{Mmig} \approx 0.25$, for x=0.

E. Slab

As previously noted, we expect that $f_{th}(surf) < f_{th}(bulk)$, where $f_{th}(surf)$ refers to the threshold for any type of atomic rearrangement. Despite the significance of surface effects, the vast number of possible surface orientations and terminations precludes any comprehensive treatment. Instead, we have performed simulations for an idealized $Li_{2(1-f)}MnO_3$ slab to identify possible surface phenomena, and to contrast them with bulk simulations. A 17-layer slab (with the slab normal perpendicular to the layers) was constructed with layer sequence

½ LM|O|L|O|LM|O|L|O|LM|O|L|O|LM|O|L|O| ½ LM (5)

The center layer composition, as well as that of the top and bottom termination layers, is $LiMn_2$. The factors of ½ indicate half-occupancy of the termination layer lattice sites (the other termination-layer sites are vacant), which preserves stoichiometry. The fully-lithiated slab contained 192 atoms. Periodically repeated slabs in the z-direction are separated by 10 Å.

After static relaxation, Mn and O at the slab surfaces spontaneously reorganize into tetrahedral Mn-O complexes. Since this process occurs without delithiation, we can regard $f_{th}(surf)$ essentially as zero. A possible consequence of this rearrangement is the availability of the pentavalent oxidation state for tetrahedral Mn upon delithiation.

Dynamical simulations were performed for the relaxed slab (with tetrahedral Mn at the slab surfaces) at 1000K. We follow a protocol for delithiation similar to that for the bulk calculations: a fraction of the Li ions in the Li layers are removed, and the slab is then relaxed statically prior to the dynamical simulations. Some surface O ions sublimate and lose contact with the slab.

We considered first the removal of 1/4 the Li ions from the Li layers, which corresponds to f=3/16. At this level of delithiation, dynamical simulation showed no dimerization in the interior layers of the slab, consistent with the results of bulk simulations [8][8], in which no dimerization was observed at this level of delithiation. A near surface oxygen ion was observed to detach (sublimate) from the slab after several ps. When the delithiation was increased to f=3/8, at which the bulk is still stable, the surface

oxygen is further destabilized, and four oxygen ions were found to detach from the surface.

The loss of surface oxygen upon delithiation of Li_2MnO_3 is, of course, expected behavior. Surface doping offers an approach to protect the oxygen. To investigate the effect of doping, Mn ions in the slab termination layers were replaced by Ru ions, so that the composition of those layers was $LiRu_2$. Ru, as well as some other polyvalent elements, may inhibit oxygen instability by assuming oxidation states greater than four. No oxygen detachment was observed in dynamical simulations for the Ru-substituted slab.

The results of this section are unavoidably somewhat anecdotal, because systematic treatment of surfaces would be prohibitive. However, the results confirm that atomic rearrangements occur at the surface at lower delithiation levels than in the bulk. At the surface, rearrangement to form tetrahedral Mn may occur. Further rearrangement, with loss of oxygen, and possible oxidation of Mn to 5+ may occur upon delithiation.

IV. Discussion

The goal of this work is to characterize the instability of $x\mathrm{Li}_{2(1-f)}\mathrm{MnO}_3\bullet(1-x)\mathrm{Li}_y M\mathrm{O}_2$ with respect to oxygen dimerization and Mn migration during the first charge. When the charge is extended deep into the voltage plateau (f greater than about ¾), the density of dimers n_{dim} and of migrated Mn ions n_{Mmig}, are of the order of a few tenths, with some variation depending on the composition of M. These values are extremely high compared to typical vacancy and interstitial densities in crystalline solids, and defect densities at this level imply that the crystalline order of the Li_2MnO_3 domains in the pristine material is essentially destroyed by activation; with such extensive disorder, atomic reversibility upon cycling is expected to be limited, at best. We suggest that the consequences of such destruction, particularly *VF*, would likely be unacceptable in a commercial product, and that research on the Li-rich layered materials should therefore be directed at developing materials and operating protocols that preserve the ordering in the pristine material as much as possible.

At present, an understanding is lacking of the interplay between the atomic scale disorder created by transformations at the surface, on one hand, and in the bulk, on the other, during the first charge, and how they combine to create lower-energy-density phases such as spinel that are responsible for the observed *VF*. Although the detailed relationship between the macroscopic property of *VF* and the microscopic properties accessible to simulation is unknown, empirical evidence[29] suggests that voltage fade is roughly proportional to $V_c - V_a$, where V_c is the upper cutoff voltage, which is related to the delithiation fraction f:

$$f = \alpha\,(V_c - V_a), \qquad (6)$$

where $\alpha \approx 2$. To maximize capacity and energy density, a high V_c is desirable. We believe that a prudent choice of V_c would correspond to $f < f_{\mathrm{th}}(\mathrm{bulk}) = 3/8$, or $V_c \approx 4.6$. For this choice, the oxygen dimer creation and Mn migration in the bulk would be largely suppressed, and the capacity

$$Q_{\max} \approx 2x f_{th}(\mathrm{bulk}) + (1-x)\,(1-y), \qquad (7)$$

per formula unit, or about 200 mAh/g, for x=0.4, and y=0, a respectable value, which could be achieved with relatively low Ni content.

For such operation to be essentially *VF*-free, however, would require stabilization of the surface against oxygen loss, dimerization, etc., at the selected V_c, as well as suppression of the related processes that result in spinel creation with cycling. To achieve such stabilization would require, in effect, strengthening the cubic-close-packed oxygen sublattice that underlies the Li-rich materials. Most vulnerable are the Li_2MnO_3 domains, for which the oxygen sublattice in the charged system is held intact mainly by crystal field stabilization. Protection of the oxygen sublattice might be accomplished, for example, by coating $x\mathrm{Li}_2\mathrm{MnO}_3\bullet(1-x)\mathrm{Li}M\mathrm{O}_2$ with $LiMn_{1.5}Ni_{0.5}O_4$. Other approaches, based on doping (cf. section III E), or gradient structures also come into consideration. A negative gradient of the Li_2MnO_3 component towards the surface might be effective, if the oxygen sublattice in the $LiMO_2$ component were more robust at high voltage than that of Li_2MnO_3.

The approach suggested here runs contrary to the one that has been widely followed[3] in attempts to mitigate *VF*: operate with $V_c \approx 4.8$ to maximize capacity, and attempt to control *VF* by tuning various cell feature and compositions. Some types of coatings[3] have indeed yielded *VF* as low as 0.6 mV. However, even this relatively low value is likely still well above what would be tolerable in a commercial product. Moreover, even if this number can be lowered further, the accompanying material degradation might defeat its practical usefulness for reasons other than energy density loss, such as impedance increase.

VI. Conclusion

A viewpoint is presented, and supported in part by simulation, on first-charge transformations in the Li-rich layered cathode materials. We suggest that reduction in *VF* would require protection of the oxygen sublattice at the surface against transformations such as dimerization and evolution. If this viewpoint is correct, a possible approach to making Li-rich layered cathode materials viable would involve (i) surface engineering to increase f_{th}(surface), and, (ii) restricting the delithiation fraction f of $Li_{2(1-f)}MnO_3$ to values below f_{th}(bulk). The success of such a program is clearly not guaranteed, but the program has the virtue of being guided by our current understanding of the microscopic processes responsible for voltage fade.

Acknowledgments
Support from the Battery Materials Research (BMR) Program, U.S. Department of Energy, Office of Energy Efficiency and Renewable Energy, is gratefully acknowledged. The submitted manuscript has been created by UChicago Argonne, LLC, Operator of Argonne National Laboratory ("Argonne"). Argonne, a U.S. Department of Energy Office of Science laboratory, is operated under Contract No. DE-AC02-06CH11357. Computer time allocations at the Fusion Computer Facility, Argonne National Laboratory, is gratefully acknowledged. This research used resources of the National Energy Research Scientific Computing Center, which is supported by the Office of Science of the U.S. Department of Energy under Contract No. DE-AC02-05CH11231.

References

1. Lu, Z.; Dahn, J. R., Understanding the Anomalous Capacity of Li /Li [$Ni_xLi_{(1/3-2x/3)}Mn_{(2/3-x/3)}$]$O_2$ Cells Using in Situ X-Ray Diffraction and Electrochemical Studies. *J. Electrochem. Soc.* **2002**, *149*, A815-A822.
2. Thackeray, M. M.; Kang, S.-H.; Johnson, C. S.; Vaughey, J. T.; Benedek, R.; Hackney, S. A., Li_2MnO_3-Stabilized $LiMO_2$ (M = Mn, Ni, Co) Electrodes for Lithium-Ion Batteries. *J. Mater. Chem.* **2007**, *17*, 3112-3125.
3. Wang, J.; He, X.; Paillard, E.; Laszczynski, N.; Li, J.; Passerini, S., Lithium- and Manganese-Rich Oxide Cathode Materials for High-Energy Lithium Ion Batteries. *Adv. Energy Mater.* **2016**, *6*, 1600906.
4. Zhao, Y.; Liu, J. T.; Wang, S. B.; Ji, R.; Xia, Q. B.; Ding, Z. P.; Wei, W. F.; Liu, Y.; Wang, P.; Ivey, D. G., Surface Structural Transition Induced by Gradient Polyanion-Doping in Li-Rich Layered Oxides: Implications for Enhanced Electrochemical Performance. *Adv. Functional Mater.* **2016**, *26*, 4760-4767.
5. Gallagher, K. G.; Croy, J. R.; Balasubramanian, M.; Bettge, M.; Abraham, D. P.; Burrell, A. K.; Thackeray, M. M., Correlating Hysteresis and Voltage Fade in Lithium- and Manganese-Rich Layered Transition-Metal Oxide Electrodes. *Electrochem. Commun.* **2013**, *33*, 96-98.
6. Andre, D.; Kim, S. J.; Lamp, P.; Lux, S. F.; Maglia, F.; Paschos, O.; Stiaszny, B., Future Generations of Cathode Materials: An Automotive Industry Perspective. *J. Mater. Chem. A* **2015**, *3*, 6709-6732.
7. Croy, J. R.; Iddir, H.; Gallagher, K.; Johnson, C. S.; Benedek, R.; Balasubramanian, M., First-Charge Instabilities of Layered-Layered Lithium-Ion-Battery Materials. *Phys. Chem. Chem. Phys.* **2015**, *17*, 24382-24391.
8. Iddir, H.; Bareno, J.; Benedek, R., Stability of Li- and Mn-Rich Layered-Oxide Cathodes within the First-Charge Voltage Plateau. *J. Electrochem. Soc.* **2016**, *163*, A1784-A1789.
9. Yoon, W.-S.; Balasubramanian, M.; Chung, K. Y.; Yang, X.-Q.; McBreen, J.; Grey, C. P.; Fischer, D. A., Investigation of the Charge Compensation Mechanism on the Electrochemically Li-Ion Deintercalated $Li_{1-x}Co_{1/3}Ni_{1/3}Mn_{1/3}O_2$ Electrode System by Combination of Soft and Hard X-Ray Absorption Spectroscopy. *J. Amer. Chem. Soc.* **2005**, *127*, 17479-17487.
10. Mizokawa, T.; Wakisaka, Y.; Sudayama, T.; Iwai, C.; Miyoshi, K.; Takeuchi, J.; Wadati, H.; Hawthorn, D. G.; Regier, T. Z.; Sawatzky, G. A., Role of Oxygen Holes in Li_xCoO_2 Revealed by Soft X-Ray Spectroscopy. *Phys. Rev. Lett.* **2013**, *111*, 056404.
11. Petersburg, C. F.; Li, Z.; Chernova, N. A.; Whittingham, M. S.; Alamgir, F. M., Oxygen and Transition Metal Involvement in the Charge Compensation Mechanism of $LiNi_{1/3}Mn_{1/3}Co_{1/3}O_2$ Cathodes. *J. Mater. Chem.* **2012**, *22*, 19993-20000.
12. Iddir, H.; Benedek, R., First-Principles Analysis of Phase Stability in Layered–Layered Composite Cathodes for Lithium-Ion Batteries. *Chem. Mater.* **2014**, *26*, 2407-2413.
13. Seo, D. H.; Lee, J.; Urban, A.; Malik, R.; Kang, S.; Ceder, G., The Structural and Chemical Origin of the Oxygen Redox Activity in Layered and Cation-Disordered Li-Excess Cathode Materials. *Nat. Chem.* **2016**, *8*, 692-697.
14. Saubanère, M.; McCalla, E.; Tarascon, J. M.; Doublet, M. L., The Intriguing Question of Anionic Redox in High-Energy Density Cathodes for Li-Ion Batteries. *Energy Environ. Sci.* **2016**, *9*, 984-991.
15. Chen, H. R.; Islam, M. S., Lithium Extraction Mechanism in Li-Rich Li_2MnO_3 Involving Oxygen Hole Formation and Dimerization. *Chem. Mater.* **2016**, *28*, 6656-6663.
16. Iddir, H., *unpublished* **2017**.
17.Zheng, J. M.; Gu, M.; Xiao, J.; Zuo, P. J.; Wang, C. M.; Zhang, J. G., Corrosion/Fragmentation of Layered Composite Cathode and Related Capacity/Voltage Fading During Cycling Process. *Nano Lett.* **2013**, *13*, 3824-3830.
18. Reed, J.; Ceder, G.; Van Der Ven , A., Layered-to-Spinel Phase Transition in Li_XMnO_2. *Electrochem. Solid-State Lett.* **2001**, *4*, A78-A81.
19. Jarvis, K. A.; Deng, Z.; Allard, L. F.; Manthiram, A.; Ferreira, P. J., Atomic Structure of a Lithium-Rich Layered Oxide Material for Lithium-Ion Batteries: Evidence of a Solid Solution. *Chem. Mater.* **2011**, *23*, 3614-3621.
20. Iddir, H.; Key, B.; Dogan, F.; Russell, J. T.; Long, B. R.; Bareno, J.; Croy, J. R.; Benedek, R., Pristine-State Structure of Lithium-Ion-Battery Cathode Material $Li_{1.2}Mn_{0.4}Co_{0.4}O_2$ Derived from NMR Bond Pathway Analysis. *J. Mater. Chem. A* **2015**, *3*, 11471-11477.
21. Liang, C. P.; Kong, F. T.; Longo, R. C.; Kc, S.; Kim, J. S.; Jeon, S.; Choi, S.; Cho, K., Unraveling the Origin of Instability in Ni-Rich $LiNi_{1-2x}Co_xMn_xO_2$ (NCM) Cathode Materials. *J. Phys. Chem. C* **2016**, *120*, 6383-6393.

22. Lee, E., et al., Exploring Lithium-Cobalt-Nickel Oxide Spinel Electrodes for >= 3.5 V Li-Ion Cells. *ACS Appl. Mater. Interfaces* **2016**, *8*, 27720-27729.
23. Kresse, G.; Furthmüller, J., Efficient Iterative Schemes for Ab Initio Total-Energy Calculations Using a Plane-Wave Basis Set. *Phys. Rev. B* **1996**, *54*, 11169.
24. G. Kresse; Joubert, D., *Phys. Rev. B* **1999**, *59*, 1758.
25. Perdew, J. P.; Burke, K.; Ernzerhof, M., Generalized Gradient Approximation Made Simple. *Phys. Rev. Lett.* **1996**, *77*, 3865.
26. Paier, J.; Marsman, M.; Hummer, K.; Kresse, G.; Gerber, I. C.; Angyan, J. G., Screened Hybrid Density Functionals Applied to Solids. *J. Chem. Phys.* **2006**, *124*, 154709.
27. Hoang, K.; Johannes, M., Defect Physics and Chemistry in Layered Mixed Transition Metal Oxide Cathode Materials: (Ni,Co,Mn) vs (Ni,Co,Al). *Chem. Mater.* **2016**, *28*, 1325-1334.
28. Long, B. R.; Croy, J. R.; Park, J. S.; Wen, J. G.; Miller, D. J.; Thackeray, M. M., Advances in Stabilizing 'Layered-Layered' $x Li_2MnO_3 \bullet (1-x) LiMO_2$ (M=Mn, Ni, Co) Electrodes with a Spinel Component. *J. Electrochem. Soc.* **2014**, *161*, A2160-A2167.
29. Wei, Z.; Xia, Y.; Qiu, B.; Zhang, Q.; Han, S.; Liu, Z., Correlation between Transition Metal Ion Migration and the Voltage Ranges of Electrochemical Process for Lithium-Rich Manganese-Based Material. *J. Power Sources* **2015**, *281*, 7-10.
30. Momma, K.; Izumi, F. VESTA 3 for three-dimensional visualization of crystal, volumetric and morphology data. *J. Appl. Crystallogr.* **2011**, *44*, 1272-1276.

*benedek@anl.gov

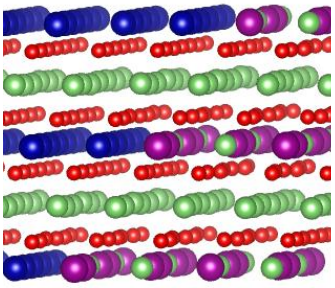

Fig. 1. Pristine structure of $0.4Li_2MnO_3 \bullet 0.6LiCoO_2$. Interfaces between $LiCoO_2$ and Li_2MnO_3 intersect the space between adjacent blue atomic rows and purple/green atomic rows. Plot created with VESTA software[30].

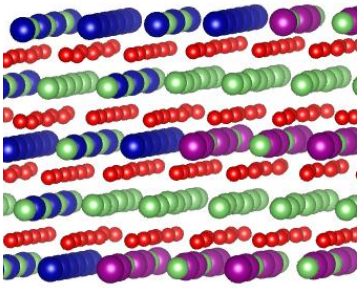

Fig. 2 Pristine structure of $0.4Li_2MnO_3 \bullet 0.3Li_2Co_2O_4$. Unlike $LiCoO_2$, ¼ of the sites in the Li layers of $Li_2Co_2O_4$ are occupied by Co. Interfaces between $Li_2Co_2O_4$ and Li_2MnO_3 intersect the space between blue (or blue/green) atomic rows and purple/green atomic rows.

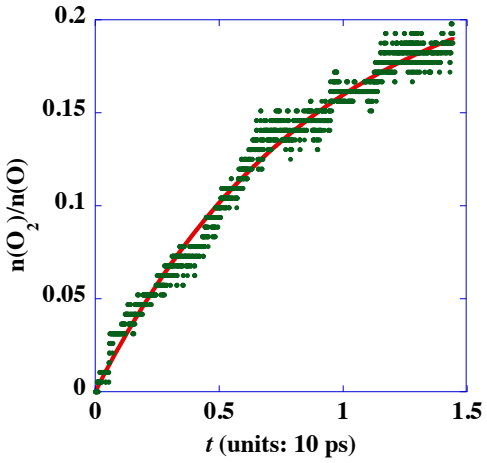

Fig. 3. Oxygen dimer density for $Li_{2(1-f)}MnO_3$, with f=3/4, simulated with first-principles molecular dynamics, fitted to Eq. (2). Time step of simulations, and those depicted in Figs. 2-4, is 1 fs.

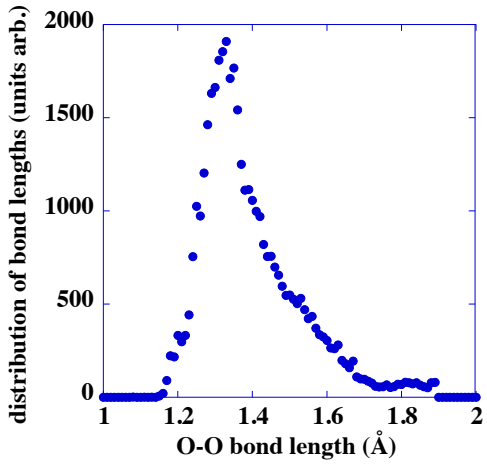

Fig. 4. Distribution of bond lengths for O-O dimers in $x\mathrm{Li}_{2(1-f)}\mathrm{MnO}_3\bullet(1-x)\mathrm{Li}_y M\mathrm{O}_2$ (in the case of M=$\mathrm{Ni}_{0.5}\mathrm{Mn}_{0.5}$, for x=0.4, f=3/4, y=0).

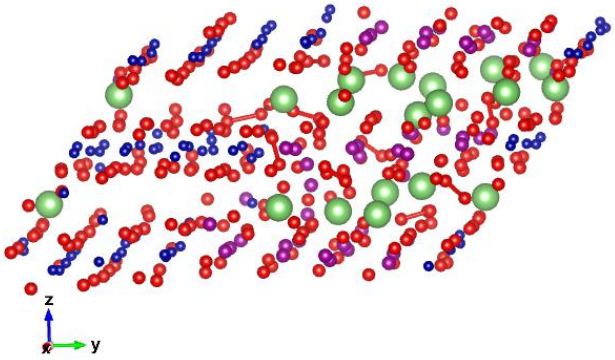

Fig. 5. Atomic configuration of $x\mathrm{Li}_{2(1-f)}\mathrm{MnO}_3\bullet(1-x)\mathrm{Li}_y\mathrm{CoO}_2$, with x=0.4, y=0.0, f=3/4, after t=5 ps. O:red; Li: green; Co: blue; Mn: purple. z-axis is perpendicular to layers. Bonds indicate O-dimers with separation less than 1.7 Å. Large y (along horizontal axis of figure): $\mathrm{Li}_2\mathrm{MnO}_3$ stripe; small y: LiCoO_2 stripe.

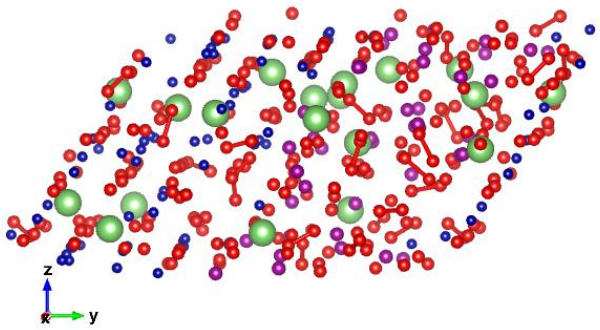

Fig. 6. Atomic configuration of $x\mathrm{Li}_{2(1-f)}\mathrm{MnO}_3\bullet(1-x)0.5\mathrm{Li}_{2y}\mathrm{Co}_2\mathrm{O}_4$, with x=0.4, y=0.0, f=3/4, after t=5 ps.

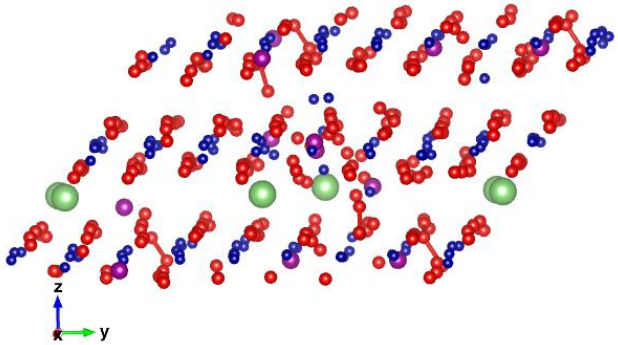

Fig. 7. Atomic configuration of $x\mathrm{Li}_{2(1-f)}\mathrm{MnO}_3\bullet(1-x)\mathrm{Li}_y\mathrm{CoO}_2$, with x=0.1, f=3/4, y=0, after t = 5 ps.

TOC Graphic